Computational aeroelastic studies of a generic hypersonic vehicle

B. J. Thuruthimattam **P. P. Friedmann** **K. G. Powell**
peretzf@umich.edu
University of Michigan, Ann Arbor,
Michigan
USA.

R. E. Bartels
NASA Langley Research Center,
Hampton, Virginia
USA.

ABSTRACT

The hypersonic aeroelastic problem of a generic hypersonic vehicle having a lifting-body type fuselage and canted fins is studied using third order piston theory and Euler aerodynamics. Computational aeroelastic response results are used to obtain frequency and damping characteristics, and compared with those from piston theory solutions for a variety of flight conditions. Aeroelastic behavior is studied for the range of 2·5 < M < 28, at altitudes ranging from 10,000ft to 80,000ft. Because of the significant computational resources required, a study on optimal mesh selection was first carried out for use with Euler aerodynamics. The three dimensional flow effects captured using Euler aerodynamics was found to lead to significantly higher flutter boundaries when compared to those based on nonlinear piston theory. The results presented here illustrate some of the more important three dimensional effects that can be encountered in hypersonic aeroelasticity of complex configurations.

NOMENCLATURE

c	reference length of geometry
C_{M_y}	coefficient of moment about the *y-axis*
C_p	coefficient of pressure
k_ω	reduced frequency
M	free stream Mach number
M, K	generalised mass and stiffness matrices of the structure
M_f	flutter Mach number
n_m	number of modes used
p	pressure
Q	generalised force vector for the structure
Q_i	generalised force corresponding to mode i
q	vector of modal amplitudes
q	dynamic pressure
q_i	modal amplitude of mode i
S	surface area of the structure
T_E	kinetic energy of the structure
T	time
U_E	potential energy of the structure
V	free stream velocity
$w(x,y,t)$	displacement of the structural surface in the z-direction
x, y, z	spatial co-ordinates
Δ_k	non-dimensional grid spacing
ω	modal frequency
ϕ_i	mode shape for mode i
ρ	air density
ζ	damping ratio
$\dot{()}$, $\ddot{()}$	first and second derivatives wrt. time

Paper No. 3340. Manuscript received 26 August 2008, accepted 28 October 2009.

https://doi.org/10.1017/S0001924000003420 Published online by Cambridge University Press

1.0 INTRODUCTION AND PROBLEM STATEMENT

Hypersonic aeroelasticity and aerothermoelasticity was a vibrant and active area of research in the late 1950s and during the 1960s as evident from Refs 1-4. This research has been instrumental in providing the basis for the aerothermoelastic design of the space shuttle. For a considerable time period afterwards, there was only limited interest in this area until the advent of the National AeroSpace Plane (NASP).

In recent years, renewed activity in hypersonic flight research has been stimulated by the need for a low cost, reusable launch vehicles and the recently completed Hyper-X programme at NASA. Other activities are focused on the design of unmanned hypersonic vehicles that meet the needs of the US Air Force. The present study is aimed at illustrating the aeroelastic behavior of a complex three dimensional hypersonic vehicle.

Vehicles in this category are based on a lifting body design. However, stringent minimum-weight requirements imply a degree of fuselage flexibility. Aerodynamic surfaces, needed for control, are also flexible. Furthermore, to meet the requirement of a flight profile that spans the Mach number range from 0 to 25, the vehicle must withstand severe aerodynamic heating. These factors combine to produce unusual aeroelastic problems that have received only limited attention in the past. Furthermore, it is important to emphasise that testing of aeroelastically scaled wind tunnel models, a conventional practice in subsonic and supersonic flow, is not feasible in the hypersonic regime. Thus, the role of aeroelastic simulations is more important for this flight regime than in any other flight regime.

Previous studies in this area can be separated into several groups. The first group consists of studies focusing on panel flutter, which is a localised aeroelastic problem representing a small portion of the skin on the surface of the hypersonic vehicle.

Hypersonic panel flutter has been studied by a number of researchers, focusing on important effects such as aerodynamic heating[5] composite[6,7] and nonlinear structural models,[8] and initial panel curvature[9]. It was noted in Ref. 9 that piston theory may not be appropriate for the hypersonic regime and that hypersonic studies might have to use unsteady aerodynamic loads based on the solution of the Navier-Stokes equations. A comprehensive review of this research can be found in a recent survey paper[10].

The second group of studies in this area was motivated by a previous hypersonic vehicle, namely the NASP[11-17]. However, some of these studies dealt with the transonic regime, because it was perceived to be quite important. Spain *et al*[12] carried out a flutter analysis of all-movable NASP-like wings with slab and double-wedge airfoils. They found that using effective shapes for the airfoils obtained by adding the boundary layer displacement thickness to the airfoil thickness improved the overall agreement with experiments. Aerothermoelastic analyses of NASP-like vehicles found that aerodynamic heating lowered the aeroelastic stability of the vehicle through the degradation of material properties and introduction of thermal stresses[15-17]. Reference 17 also found that a flutter suppression control law more than recovered the cold structure flutter boundary using normal acceleration feed¬backs and conventional control surfaces.

The third group of studies focused on hypersonic configurations such as the X-33 or the X-34. Reference 18 considered the X-34 launch vehicle in free flight at M = 8·0. The study reinterpreted the results at different flight conditions using dynamic pressure corrections, and found instabilities at speeds above M = 5·0 in the primary bending modes due to the control system. The aeroelastic instability of a generic hypersonic vehicle resembling the X-33 was considered in Ref. 19. It was found that third order piston theory is needed for the correct prediction of the hypersonic flutter boundary.

A CFD-based flutter analysis was used for the aeroelastic analysis of the X-43 configuration, using system-identification based order reduction of the aerodynamic degrees of freedom[20]. Both the structure and the fluid were discretised using the finite element approach. It was shown that piston theory and ARMA Euler calculations predicted comparable results.

From the studies on various hypersonic vehicles[11, 20-22], one can identify operating envelopes for each vehicle. A graphical representation of these operating conditions is shown in Fig. 1.

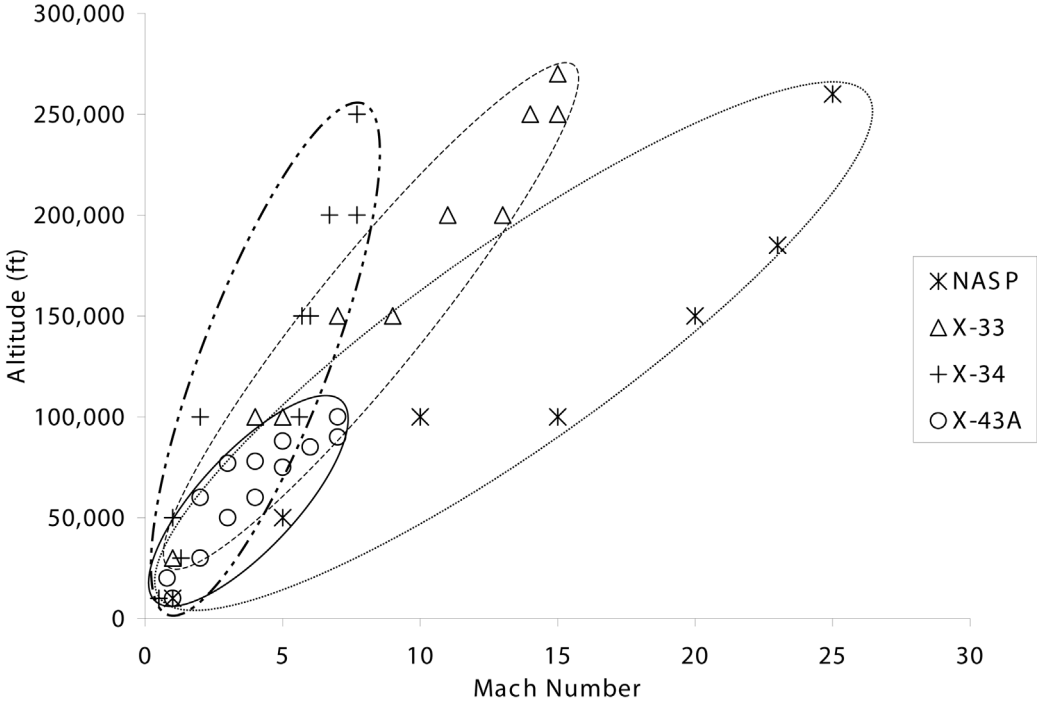
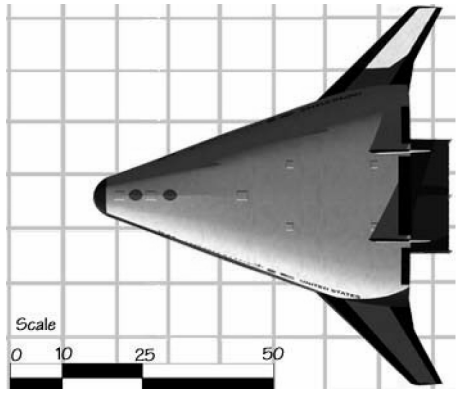


Figure 1. Operating envelopes for several modern hypersonic vehicles.

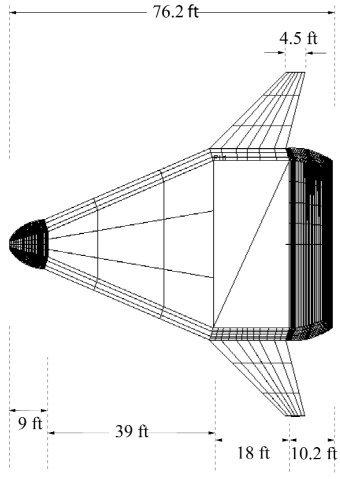
https://doi.org/10.1017/S0001924000003420 Published online by Cambridge University Press

A comprehensive survey of the research on the aeroelastic and aerothermoelastic behavior of hypersonic vehicles has been presented in Ref. 23. A detailed study of the aeroelastic and aerothermoelastic behavior of a low aspect ratio wing, representative of a fin or control surface of a hypersonic vehicle has been presented in Ref. 24. In this study the aeroelastic stability boundaries of the fin with a double wedge cross section were evaluated using three different types of unsteady aerodynamic loads: (1) third order piston theory, (2) unsteady loads based on the CFD solution of the Euler equations and (3) unsteady loads based on the CFD solution of Reynolds averaged Navier Stokes (RANS) equations. The third order piston theory solutions were based on a code developed at the University of Michigan[23] while the CFD solution utilised the CFL3D code developed at NASA Langley Research Center. It was found that the aeroelastic stability boundaries of the low aspect ratio wing using third order piston theory and Euler equations were very similar. The flutter Mach number and dynamic pressure at the flutter boundary were within 5 and 8%, respectively. Furthermore, for this case viscosity did not appear to be significant, since the flutter Mach number and the dynamic pressure at flutter, based on the solutions of the unsteady RANS equations was between 8 and 10%, respectively, compared to the Euler solutions, at an altitude of approximately 70,000ft. This behavior was attributed to the relatively low reduced frequencies associated with these cases, which imply that quasi-steady approximations, such as third order piston theory, will produce results with an acceptable level of accuracy.

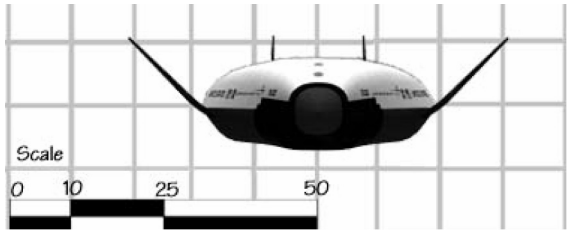
Taking advantage of these results the objective of this paper is to examine the overall behavior of a complete generic hypersonic vehicle using third order piston theory and unsteady Euler aerodynamics. The generic hypersonic vehicle considered here is derived from the X-33 vehicle which was modified so as to have a somewhat simpler configuration as shown in Fig. 2. An examination of the flutter boundaries obtained shows that three dimensional effects associated with this complex vehicle can produce larger differences between the approximate flutter boundaries based on third order piston, and Euler aerodynamics than those observed for the low aspect ratio wing considered in Ref. 24.



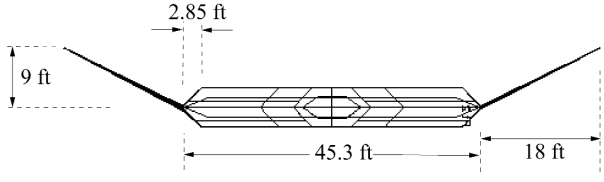
(a) X-33, top view



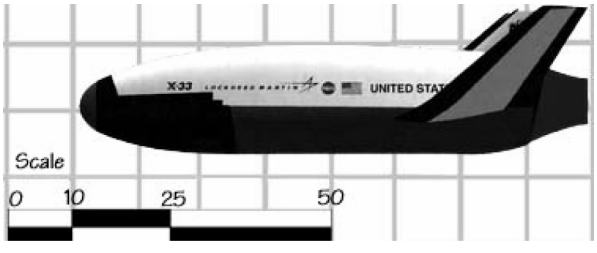
(b) Generic vehicle, top view



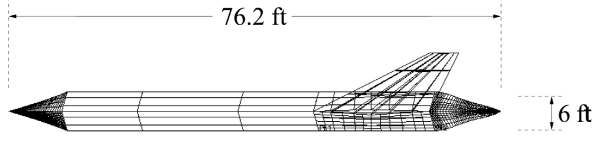
(c) X-33, front view



(d) Generic vehicle, front view



(e) X-33, side view



(f) Generic vehicle, side view

Figure 2. X-33 and generic vehicle configurations.

https://doi.org/10.1017/S0001924000003420 Published online by Cambridge University Press

2.0 METHOD OF SOLUTION

The computational aeroelastic solutions in the present study are obtained using the NASA Langley code CFL3D[25]. Specifically, the CFL3D code is used to generate both steady and unsteady air loads, and it also produces the aeroelastic transients and response solutions. The fluid–structure coupling in the code is accomplished using the free-vibration modes of the vehicle. A detailed description of the solution process is provided next.

2.1 Euler/Navier–Stokes solver in CFL3D

The CFL3D code employs an implicit finite volume algorithm based on upwind-biased spatial differencing to solve the time dependent Euler and Reynolds-averaged Navier–Stokes equations.

Multigrid and mesh sequencing are available for convergence acceleration. The algorithm, which is based on a cell-centered scheme, uses upwind-differencing based on either flux-vector splitting or flux difference splitting and can sharply capture shock waves. For applications using the thin-layer Navier–Stokes equations, different turbulence models are available. For time accurate problems using a deforming mesh, an additional term accounting for the change in cell volume is included in the time discretisation of the governing equations[26]. Because CFL3D is an implicit code using approximate factorisation, linearisation and factorisation errors are introduced at every time step. Hence, intermediate calculations (referred to as subiterations) are used to reduce these errors. Increasing these subiterations improves the accuracy of the simulation, albeit at increased computational cost.

2.2 Aeroelastic option in CFL3D

The aeroelastic approach underlying the CFL3D code is similar to that described in Refs 27 and 28. The equations are derived by assuming that the general motion $w(x, y, z, t)$ of the structure is described by a finite modal series given by Equation (1). The functions $\phi_i(x, y, z)$represent the free-vibration modes of the vehicle, which are calculated using a finite element approach:

$$w(x,y,z,t)=\sum_{i=1}^{n_m} q_i(t)\phi_i(x,y,z) \qquad ...(1)$$

The aeroelastic equations of motion are obtained from Lagrange's equations:

$$\frac{\mathrm{d}}{\mathrm{d}t}\left(\frac{\partial T_E}{\partial \dot{q}_i}\right)-\frac{\partial T_E}{\partial q_i}+\frac{\partial U_E}{\partial q_i}=Q_i\,, \qquad i=1,2,.....,n_m \qquad ...(2)$$

which yield

$$\mathbf{M}\ddot{\mathbf{q}}+\mathbf{K}\mathbf{q}=\mathbf{Q}(\mathbf{q},\dot{\mathbf{q}},\ddot{\mathbf{q}}), \qquad q^T=[q_1,q_2,....,q_m] \qquad ...(3)$$

Where the elements of the generalised force vector are given by

$$Q_i=\frac{\rho V^2 c^2}{2}\int_S \phi_i \frac{\Delta p(\mathbf{q},\dot{\mathbf{q}},\ddot{\mathbf{q}})\,dS}{\left(\frac{\rho V^2 c^2}{2}\right)} \qquad ...(4)$$

The aeroelastic equations are written in terms of a linear state-space equation (using a state vector of the form $[...\dot{q}_{i-1}\ q_i\ \dot{q}_i\ q_{i+1}]$ such that the modified state-transition-matrix integrator can be used to march the coupled fluid-structural system forward in time. At the beginning of each time step, the incremental structural deflections are calculated using modal velocities and generalised aerodynamic forces. Using a deforming mesh the mesh points are moved so that the inner mesh boundaries conform to the new deformed shape of the structure and far field boundaries are held stationary. The fluid equations, including the geometric conservation law terms, compute the flow field throughout the updated mesh. The generalised aerodynamic forces acting on the structure through the next time step are then computed. Thus, tight coupling of the flow and the structure are implemented through the generalised aerodynamic forces. Finally, a time history of the modal displacements, modal velocities, and generalised forces is obtained.

2.3 Fluid-structure coupling

Prediction of the dynamic response of a flexible structure in a fluid requires the simultaneous solutions of the equations of motion of the structure and the fluid. In order to impose the kinematic boundary conditions on the fluid mesh at the new time step, the location and velocity of the fluid-structure boundary must first be known. This requires the solution of the entire system of equations for the structure, a task which cannot be carried out till the current surface pressure is known, which depends on the solution of the fluid domain and thus also on the unknown boundary conditions during the current time step. In addition, the discretised model of the structure uses a Lagrangian approach by following a point located on the structure over time, while the discretised model of the fluid uses an Eulerian approach by computing the flow quantities at a specific location in space over time. Therefore, accurate coupling of the two systems is a complicated endeavor. A straightforward approach to the solution of the coupled fluid-structure system requires changing the fluid grid at each time-step, which is computationally very expensive. Therefore, several different approaches have emerged as alternatives to partial regridding in transient aeroelastic computations, among them being dynamic meshes[29], the space-time formulation[30-32], the Arbitrary/Mixed Eulerian-Lagrangian formulation[33, 34], the multiple-field formulation[35, 36] and the transpiration method[20,37].

This study implements the exponential-decay/transfinite interpolation (TFI) approach[38, 39], which is an algebraic mesh deformation method in which surface movement is transmitted into the mesh interior using an exponential-decay function. The motion of selected slave points, chosen across a grid at constant index intervals, is tied to the motion of the nearest surface (or master) point. The exponential-decay function uses distance between the slave and nearest surface point so that motion of the surface is transmitted nearly undiminished to nearby slave points. Intervening mesh points on block faces are updated using TFI, a scheme[40, 41] that efficiently maps grid displacements from one block face to another using polynomial functions. Once the intermediate mesh between slave points is updated on block faces, block interiors are updated using a volume TFI step. When smoothing of the deformed grid is necessary, several iterations of a modified spring analogy are employed. This scheme is a modification of the spring analogy[28] by using axial spring stiffness. Spring stiffness in the mesh interior is controlled by the spacing of the appropriate boundary grid points. Note that the axial stiffness approach results in smoothing of the mesh and also allows adaptation based on the flow solution. Furthermore, the problem of grid collapse around convex surfaces is handled by selectively increasing/decreasing stiffness based on surface curvature. Note that during the mesh deformation process, the code ensures that the generated control points at block boundaries are coincident and also checks block boundaries for separation during the mesh deformation at each time step[39].

https://doi.org/10.1017/S0001924000003420 Published online by Cambridge University Press

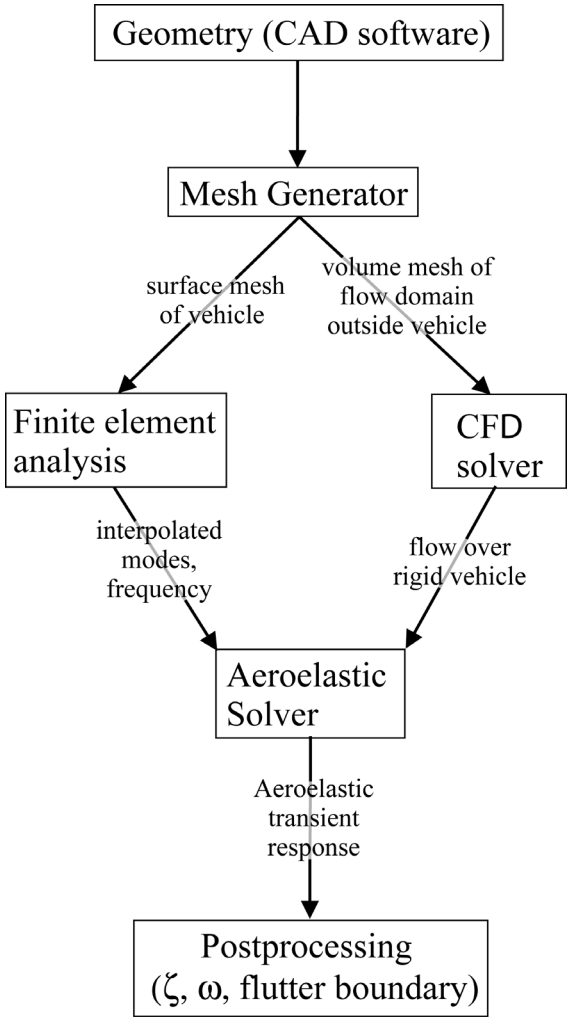


Figure 3. A flow diagram of the computational aeroelastic solution procedure.

3.0 GENERAL OVERVIEW OF THE SOLUTION PROCESS

The solution of the computational aeroelasticity problem used in the present study is shown in Fig. 3. First, the vehicle geometry is created using CAD software, and from this geometry a mesh generator is used to create a structured mesh for the flow domain around the body. In parallel, an unstructured mesh is generated that represents the surface of the finite element model of the vehicle. This structural model is further refined with internal stiffeners and mass elements to represent a complete vehicle, and is used to obtain the free vibration modes of the vehicle using MSC NASTRAN[42]. Subsequently, the fluid mesh is used to compute the flow around the rigid vehicle using a CFD solver, which consists of the CFL3D code developed by NASA Langley Research Center. In order to generate the aeroelastic input for CFL3D, the modal deformation at each surface gridpoint in the fluid mesh is obtained by using cubic interpolation (in MATLAB) from the finite element structural model, for each structural mode. Using the flow solution as an initial condition, and the interpolated modal data as additional input, an aeroelastic equilibrium state is obtained for the flexible vehicle.

For a geometry with vertical symmetry at zero angle-of-attack, such as a double-wedge aerofoil, the equilibrium state is the same as the undeflected state. Next, the structure is perturbed in one or more of its modes by an initial modal velocity condition, and the transient response of the structure is obtained. To determine the flutter conditions at a given altitude, aeroelastic transients are computed at several Mach numbers and the corresponding dynamic pressures. The frequency and damping characteristics of the transient response for a given flight condition and vehicle configuration can be determined using the moving block approach, which analyses the Fourier transform of a discretely sampled transient signal[43]. This approach applied to the same altitude and vehicle configuration for a range of Mach numbers results in a series of damping values for the system. The flutter Mach number can be estimated from this series by interpolating the damping data points to identify zero damping.

3.1 Computational model for the generic hypersonic vehicle

In order to carry out aeroelastic simulations of the generic vehicle using Euler aerodynamics, various meshes were constructed for the computational domain shown in Fig. 4. Developing a suitable mesh for use with CFL3D requires balancing between various conflicting constraints.

One of the main factors deciding the usefulness of the mesh is the overall size of the mesh, which directly affects runtime. Having fixed the overall mesh size, obtaining accurate results requires having optimum placements for the internal gridpoints. This is done by having the maximum possible number of gridpoints lie within the shocks forming around the geometry. The midplane of the selected mesh is shown in Fig. 5, while Fig. 6 shows the grid points around the typical cross-section of the generic vehicle. On the surface of the generic vehicle, the gridpoints are again finely spaced close to the edges of the geometry. A more detailed description of a study on grid convergence is given in Ref. 24, where the appropriate computational domain and mesh resolution required for the hypersonic aeroelastic analysis of a low aspect-ratio wing were determined.

By varying the nondimensional grid-spacing, representing the distance of the closest grid-point in the normal direction, different pressure distributions on the surface of the fin at 75% of span were obtained, in order to assess convergence. The grid size of 3×10^6 gridpoints, the gridpoint placement on the surface and all other grid parameters were kept constant for these simulations. As seen in Table 1, the error in the moment acting on the typical section was reduced with decreasing Δ_k. Reference 24 indicates that the maximum error of 0·28% is small enough to yield converged results. However, aeroelastic simulations could not be carried out for Δ_k less than 5×10^{-7}, as this led to mesh entanglement. When this occurs, cell boundaries penetrate through adjacent cell volumes, and leads to gridlines that cross each other. In CFL3D, this leads to negative cell volumes in the region surrounding the entanglement. Reducing the time-step was found to allow the use of slightly smaller grid spacing,

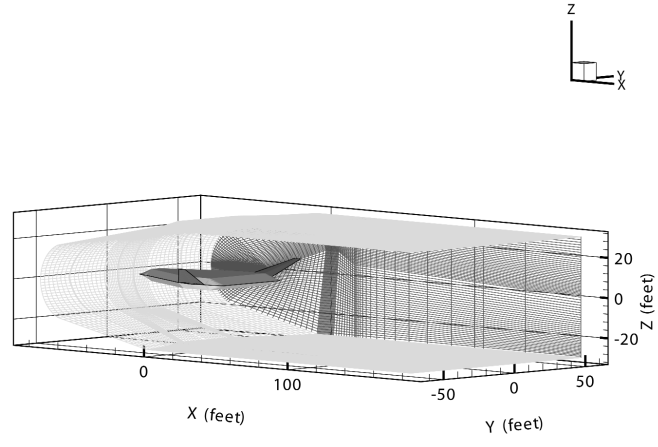


Figure 4. A view of the generic vehicle and CFD domain around it.

https://doi.org/10.1017/S0001924000003420 Published online by Cambridge University Press

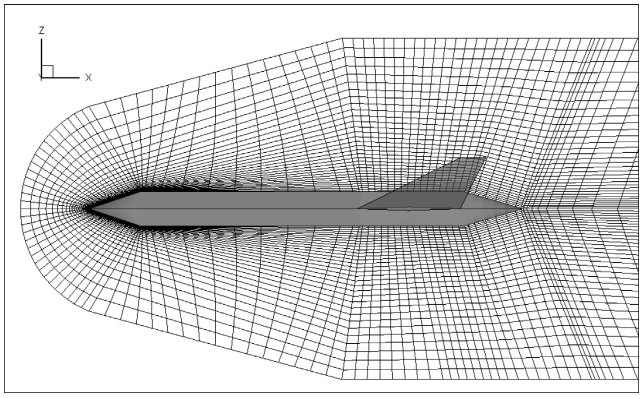


Figure 5. A view of the mid plane of the grid around the generic vehicle.

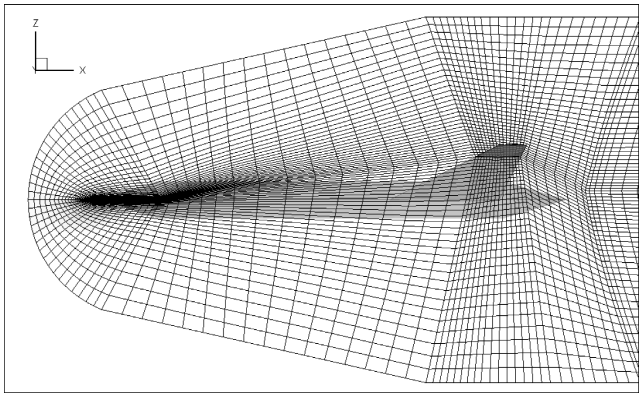


Figure 6. A view of the grid around the typical cross-section of the generic vehicle.

but with a significant increase in computational time. Hence, the time-step size was selected to be $\Delta t = 0{\cdot}35 \times 10^{-3}$ sec, which allows accurate calculation of the aerodynamic forces, provides at least 50 time-steps per cycle of the highest frequency mode, and avoids mesh entanglement for this value of Δ_k. The above mesh was referred to as the 'fine' mesh, and for comparison, an additional mesh having 4×10^5 gridpoints was also created. This mesh is referred to as the 'coarse' mesh, and has a nondimensional grid-spacing at the surface in the coarse grid of $\Delta_k = 6{\cdot}5 \times 10^{-6}$.

The coarse mesh is a $65 \times 177 \times 33$ C-grid with 177 points around the vehicle and its wake, 65 points spanning the grid from side to side, and 33 points extending radially outward from the vehicle surface. Of these, 145 points were wrapped around the fuselage in the streamwise direction, while 33 points were distributed on the vehicle fuselage from side-to-side. The fin surfaces were discretised using nine grid points in the span-wise direction and 17 grid points from leading edge to trailing edge. The refined mesh is a $129 \times 355 \times 65$ C-grid with 355 points around the vehicle and its wake, 129 points spanning the grid from side to side, and 129 points extending radi¬ally outward from the vehicle surface. Of these, 289 points were wrapped around the fuselage in the streamwise direction, while 65 points were distributed on the vehicle fuselage from side to side. The fin surfaces were discretised using 17 grid points in the span-wise direction and 33 grid points from leading edge to trailing edge. In both cases, the computational domain was extended 0·5 vehicle-length upstream and 1·5 chord lengths downstream. On either side, the domain extended 0·5 vehicle-lengths spanwise. The distance to the upper and lower boundaries was selected to be slightly larger than the shocks forming at M = 5·0, with the shocks from the nose of the vehicle flowing out of the domain boundaries without reflection.

Table 1
Error in moment calculation for typical section as a function of grid spacing

Nondimensional grid-spacing in normal direction (Δ_k)	C_{M_y}	Error(%)
2×10^{-6}	–0·1281	0·2799
2×10^{-7}	–0·1279	0·1347
1×10^{-8}	–0·1278	0·0490
1×10^{-9}	–0·1277	N/A

3.2 Structural model of the generic hypersonic vehicle

The model employed in this study is based on a lifting body-type vehicle configuration that resembles a reusable launch vehicle. The model consists of a fuselage combined with canted fins, shown in Fig. 7. The overall dimensions of the generic vehicle are 76·2ft. length, 45·54ft width, and 6ft thickness. The generic hypersonic vehicle has two canted fins, swept backwards at an angle of 32°. The fins have a root chord of 18ft, with a taper ratio of 0·25. Both fins have double-wedge cross-sections, with the maximum thickness at the center of the aerofoil section. Each fin has a thickness ratio of 3·33%, which remains constant along the span of the fin. The fins rise from the horizontal plane at an angle of 26·5°, though the angle of attack of each section is 0°. The empty weight of the vehicle is 70,000lb, and each fin weighs 386lbs.

The model has 7474 nodes, with 7486 CQUAD4 elements (bilinear plate elements) on the surface, and an additional 930 CQUAD4 elements are used to represent the internal stiffeners. Each canted fin comprises 623 CQUAD4 elements. The material properties and thickness of the plate elements are chosen to enable approximate matching of the natural frequencies with those obtained from a finite element model of another representative generic hypersonic vehicle[44]. The free vibration modes of the generic hypersonic vehicle were obtained using MSC NASTRAN, using the finite element model shown in Fig. 7. The first two modes are symmetric and anti-symmetric fin bending modes, while the higher modes involve deformations of the entire vehicle. The higher modes (modes 9 through 12) predominantly show deformations of the fins.

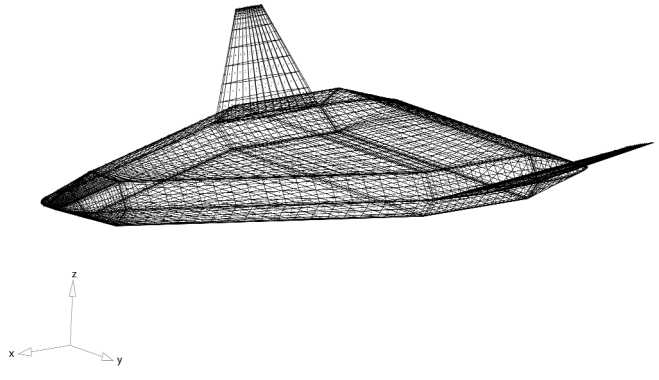


Figure 7. Finite element model of the generic reusable launch vehicle. The plane of vertical symmetry for the undeformed fuselage is the *x-y* plane.

https://doi.org/10.1017/S0001924000003420 Published online by Cambridge University Press

4.0 RESULTS AND DISCUSSION

The results presented in this section illustrate the aeroelastic behavior of a complete, and fairly complex hypersonic vehicle configuration By comparing results for Euler aerodynamics and piston theory, one can identify the effectiveness of piston theory in approximating the aeroelastic behavior of a complex three-dimensional hypersonic vehicle in inviscid flow.

Note that in the course of this research considerable effort was invested to determine the appropriate step sizes required when using the Euler and Navier-Stokes solvers in CFL3D[24].

4.1 Aeroelastic behaviour of the generic hypersonic vehicle using piston theory

Piston theory[46,47] is a simple aerodynamic theory valid for M > 2, which provides a point-function relationship between the local pressure on the surface of the vehicle and the component of fluid velocity normal to the moving surface. For three-dimensional geometries, piston theory requires initial knowledge of the inviscid flow on the surface, such as might be obtained from an Euler aerodynamic model of the generic vehicle. However, this would significantly increase the computational effort required for piston theory analysis of the vehicle. Hence, it was decided to apply the piston theory analysis to sections of the generic vehicle taken in parallel *x-z* planes, with the axes as defined in Fig. 7. Prior to studying the aeroelastic behavior for a vehicle, it is necessary to address the validity of using piston theory in a sectional manner for the flow around the vehicle. Studies of the rigid vehicle in Euler flow at M = 2·6, 8 and 25 were carried out to determine the flow field on the surface of the vehicle. It was found that at supersonic Mach numbers, the flow on top of the fuselage shows significant transverse velocity components. However, the streamlines over the canted fins show very limited deflection, the Mach number distribution over the entire fin is below free-stream, due to the effect of body flow. In contrast, at hypersonic Mach numbers, the flow over the entire vehicle shows small transverse velocity components, justifying the use of piston theory via a sectional approach. Also, the flow over the outer half of the canted fins was seen to be at free-stream conditions. Such a flow pattern is illustrated in Fig. 8, which shows the flow on the top surface of the generic vehicle, when calculated using Euler aerodynamics at M = 8·0 and 40,000ft.

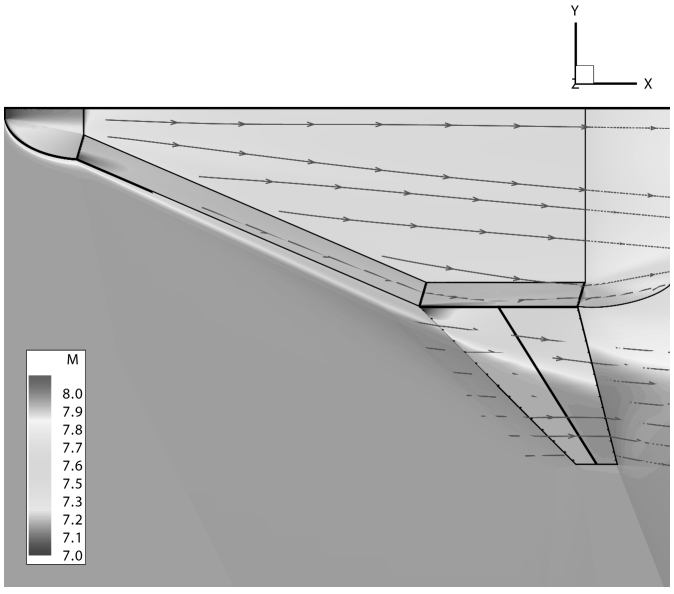


Figure 8. Flow on the top surface of the generic vehicle, with M = 8·0 and Euler aerodynamics at 40,000ft.

A convergence study for flutter at 40,000ft, using nonlinear piston theory, indicated that at least 12 modes are required for simulating the aeroelastic behavior of the generic vehicle[45].

Typical behaviour of the aeroelastic modal response is shown in Figs 9 through 11. The upper half of the figure shows the variation in damping with Mach number, for the modes which are identified by a mode number that is specified along the third axis. The flutter Mach number is obtained when any of the damping curves rises above the shaded plane, which corresponds to zero damping. The lower half of the figure shows the variation of modal frequencies with Mach number for the various modes. The frequencies of the modes at flutter are indicated by black dots. The results as obtained using nonlinear piston theory are shown in Fig. 9, with M_f = 7·1 and k_ω = 0·3106. In this case, the flutter arises from the interaction among the higher modes, which have significant fin bending. The fuselage flexural and torsional modes (modes 3 and 4) do not play a significant role in this instability.

The values of the reduced frequencies for the cases considered indicate that the use of a quasisteady approach such as piston theory appears to be justified. Note that the reduced frequencies are calculated using the vehicle length as the reference length, and would be much smaller if the root chord length of the fin were used.

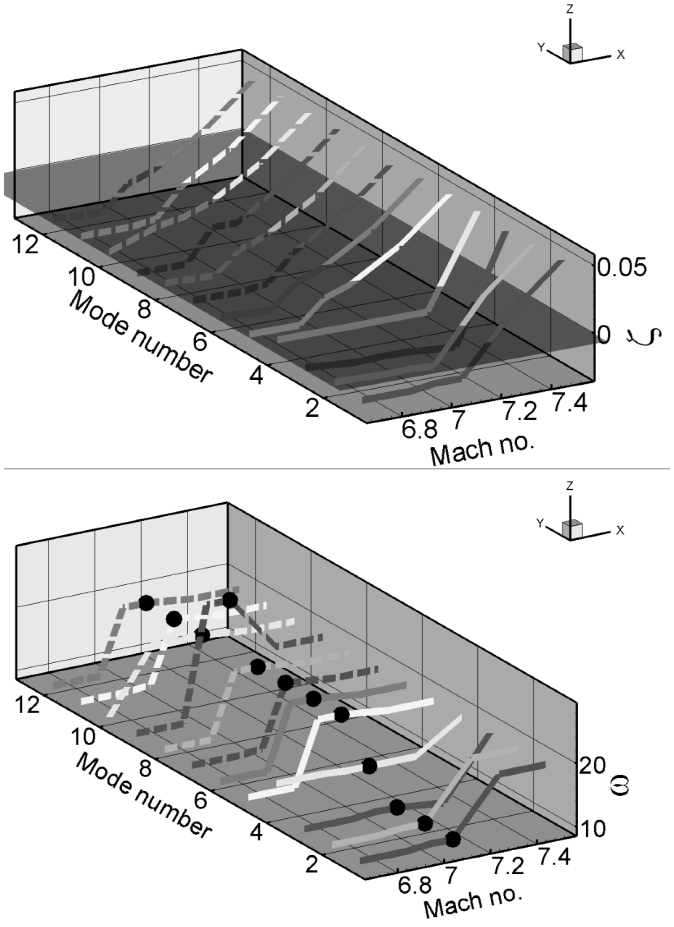


Figure 9. Aeroelastic behavior of the generic vehicle at 40,000ft, calculated using nonlinear piston theory, and 12 modes.

https://doi.org/10.1017/S0001924000003420 Published online by Cambridge University Press

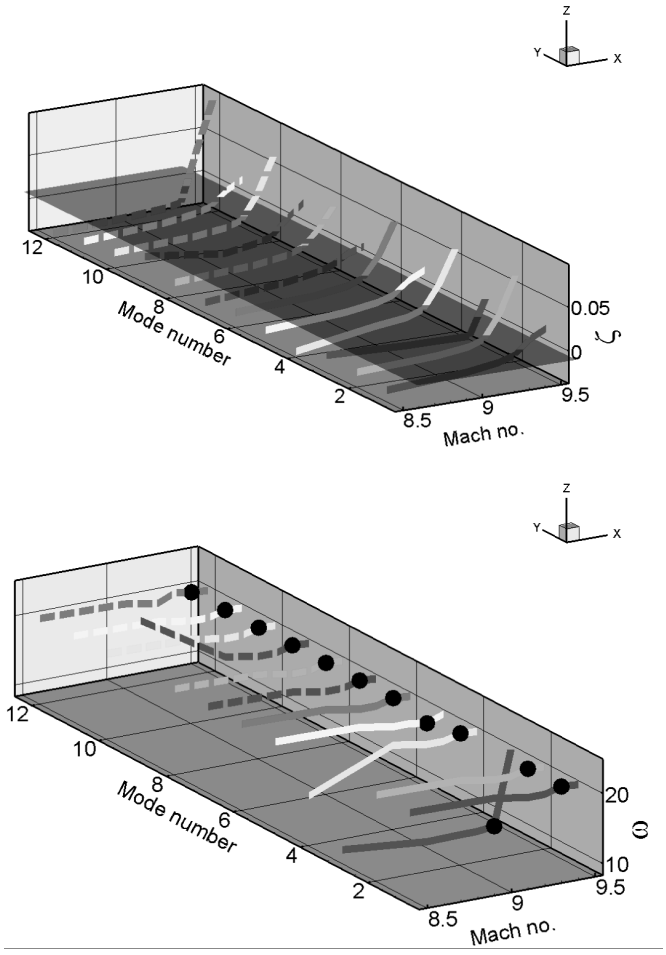


Figure 10. Aeroelastic behavior of the generic vehicle at 40,000 feet, calculated using Euler aerodynamics, and 12 modes. The calculations were carried out on the coarse mesh.

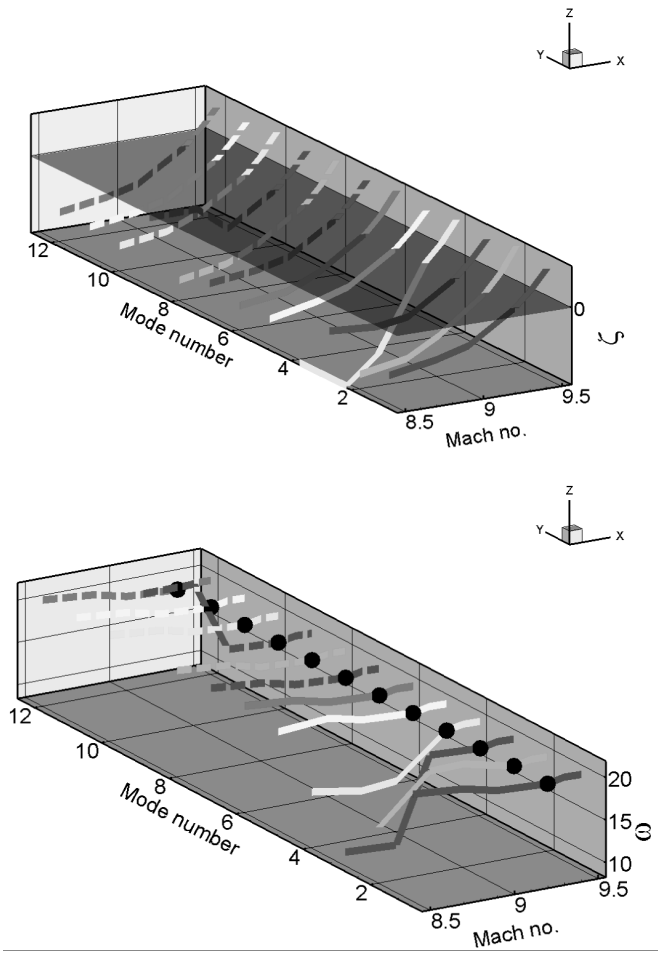


Figure 11. Aeroelastic behavior of the generic vehicle at 40,000ft, calculated using Euler aerodynamics, and 12 modes. The calculations were carried out on the fine mesh.

4.2 Aeroelastic behaviour of the generic hypersonic vehicle using Euler aerodynamics

Figures 10 and 11 present the aeroelastic behavior of the generic vehicle using Euler aerodynamics. Figure 10 shows the aeroelastic behavior of the vehicle calculated on the coarse mesh, while Fig. 11 shows the aeroelastic behavior calculated on the refined mesh. Both series of simulations predict flutter at $M_f = 9{\cdot}3$, which is 31% higher than that predicted by nonlinear piston theory. The figures also show that all modes become equally unstable as the flutter boundary is reached, though the higher modes with significant fin bending are slightly less stable. The reduced frequency at flutter obtained on the coarse mesh was $k_\omega = 0{\cdot}1714$, while that on the refined mesh was $k_\omega = 0{\cdot}1626$.

The significant difference in flutter boundaries predicted using the two aerodynamic models is due to the presence of three-dimensional flow effects. Prior to calculation of the aeroelastic transients, the aeroelastic equilibrium state of the flex-ible vehicle was calculated by allowing the vehicle to deform in hypersonic flow, with artificial structural damping (1% of critical) added to accelerate convergence. In the case of piston theory which is a two-dimensional theory, as each cross-section of the vehicle is symmetrical about the horizontal plane, the equilibrium state of the flexible vehicle is the same as the rigid geometry at zero angle-of-attack. However, Euler aerodynamics is a fully three-dimensional aerodynamic model, and the inclination of the fins leads to higher pressure on the upper surface compared to the lower surface, causing the fins to bend outwards along the span-wise direction. For inviscid flow with M = 8·0 at 40,000ft, the typical cross-section translates downward by nearly one foot. This deformation of the section is strongly dependent on the specific structural model of the fins and stiffeners.

Figure 12 depicts the typical cross-sections of a fin from rigid and aeroelastic equilibrium states in Euler flow, which are superimposed on each other. As evident from the figure, the cross-section of the flexible vehicle has deformed and it has also developed a slight angle of attack. Carrying out a linear fit to the mean line of the cross-section in Euler flow indicates an effective angle of attack of 0·3°. Figure 13 shows the surface pressures on the typical cross-sections of the rigid and flexible configurations at equilibrium in inviscid flow, and it is evident from the figure that these are quite different. Note that the surface pressure on the rigid vehicle using nonlinear piston theory is the same as that obtained using Euler aerodynamics.

The deformation of the typical cross-section from the double-wedge airfoil leads to a significantly different pressure profile of the typical section. Thus, the introduction of flexibility interacts with the three-dimensional flow captured using Euler aerodynamics to change the equilibrium configuration of the generic vehicle. In comparison, the aeroelastic equilibrium state for the vehicle is the same as the undeformed state when using piston theory. Since the aeroelastic transients are calculated by considering small perturbations about the equilibrium position, the two models yield different aeroelastic behavior.

Figure 14 depicts the contours of C_p around the typical section for the rigid vehicle at M = 8.6 and 40,000ft when using Euler aerodynamics, and Fig. 15 shows the flow around the deformed section when vehicle flexibility is introduced. Comparison the two figures indicates significant change in in C_p on and around the typical

https://doi.org/10.1017/S0001924000003420 Published online by Cambridge University Press

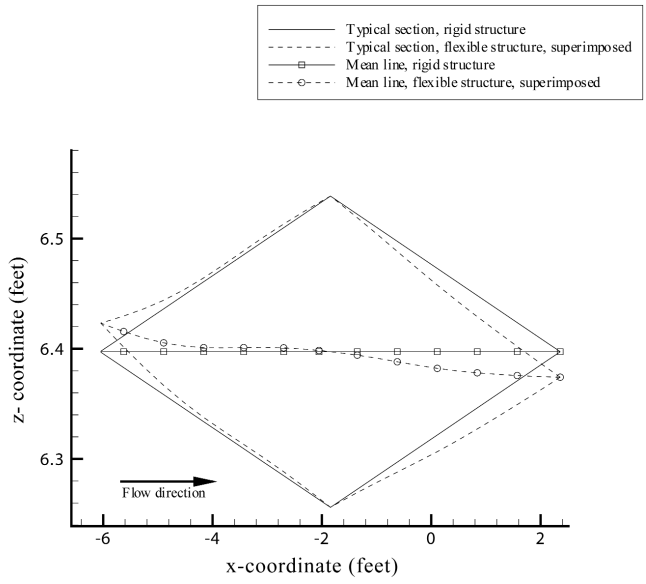


Figure 12. Superimposed views of the typical sections and mean lines for the rigid and damped equilibrium configurations of the typical cross-section. M = 8·0, 40,000ft.

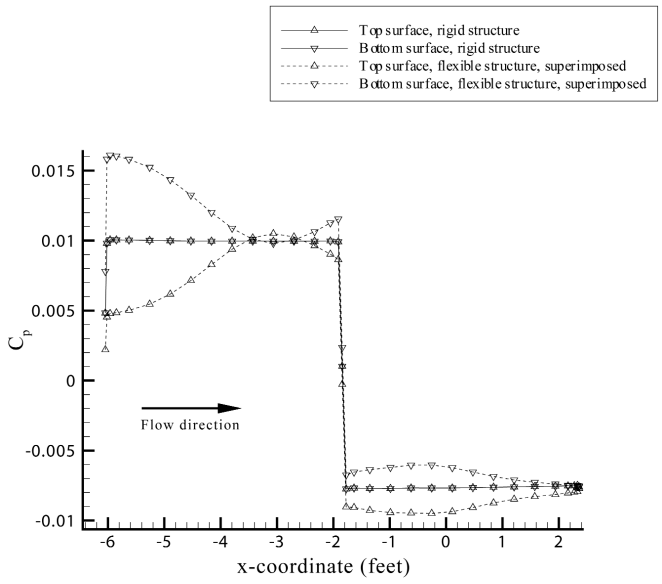


Figure 13. C_p on the surface for the rigid and damped equilibrium configurations of the typical cross-section. M = 8·0, 40,000ft.

section. Similar differences were found at M = 2·6 at 10,000ft and M = 25·0 at 70,000ft. These figures show that the deformed section leads to an asymmetric distribution of pressure on the top and bottom surfaces, especially near the leading edge. This is unlike the rigid section which has develops symmetric pressure loading on both surfaces.

For comparison, the aeroelastic simulations of the entire vehicle were also carried out using seven modes. For this incomplete representation of the generic vehicle, both piston-theory and Euler-based aeroelastic studies indicate similar flutter behavior, with flutter arising from interaction between the symmetric fin bending mode and the fuselage flexural mode. This trend of good comparison between Euler aerodynamics and piston theory follows that also observed in Ref. 24 for the low aspect-ratio wing, and Ref. 20 for the X-43 geometry. For convenient comparison, the results of all the aeroelastic simulations described in this paragraph are summarised in Table 2.

The flutter envelope for the generic vehicle, calculated using 12 modes, is shown in Fig. 16. This figure compares the flutter boundaries at various altitudes calculated using third-order piston theory, and Euler aerodynamics on the coarse and refined meshes. At low altitudes, nonlinear piston theory predicts flutter boundaries comparable with Euler aerodynamics-based methods for the generic vehicle. However, at altitudes above 30,000ft, there is a significant difference, which becomes approximately constant above 50,000ft. For the range between 10,000 and 50,000ft, for which results could be obtained, the coarse mesh also compares well with the flutter results from the refined mesh.

The differences displayed in Fig. 16 are magnified in Fig. 17, which shows a comparison of the dynamic pressure at flutter for the different altitudes considered. From this figure, it is obvious that the comparison between piston theory and Euler aerodynamics at low altitudes is not as good as seen in Fig. 16. At higher altitudes, piston theory underpredicts the flutter dynamic pressure compared to Euler aerodynamics by 25-50%. However, piston theory does indicate a similar trend, including the maximum value corresponding to 70,000 feet. Considering the Euler results on the two meshes, good comparison is observed between 10,000 and 40,000ft, while the results at 50,000ft begin to show a divergence. Results at higher altitudes could not be obtained on the coarse mesh due to the insufficiently refined grid spacing near the surface, leading to a lack of

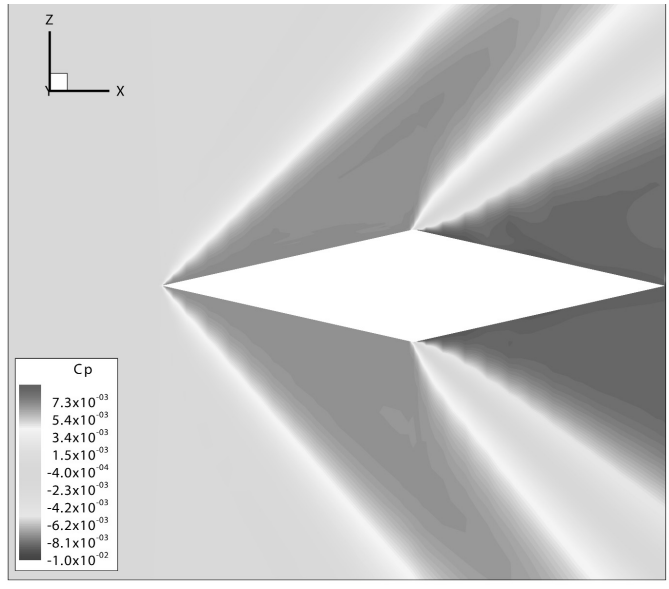


Figure 14. Pressure contours around the rigid typical section of the canted fin of the generic vehicle at M = 8·0, at 40,000ft, using Euler aerodynamics.

convergence in the flow solutions. Solutions above 80,000ft could not be obtained on the refined mesh due to a similar lack of convergence for M > 28.

Another challenge with calculating flutter boundaries at very high altitudes is the length of the transient required to identify flutter. At altitudes below 70,000ft, transients of one second have been used to identify flutter reliably. At very high altitudes, due to the rarefied atmosphere, the aeroelastic loads are quite small even at high M. Figure 18 shows the aeroelastic transients for modes one and nine, calculated at M = 28·0 and 80,000ft. The gradual increase in the amplitude of mode nine can be seen, although all the other modes were observed to be quite stable. For this flight condition, the computational resources required are an order of magnitude higher than that required for lower altitudes, since the transients have to be simulated over much longer periods.

https://doi.org/10.1017/S0001924000003420 Published online by Cambridge University Press

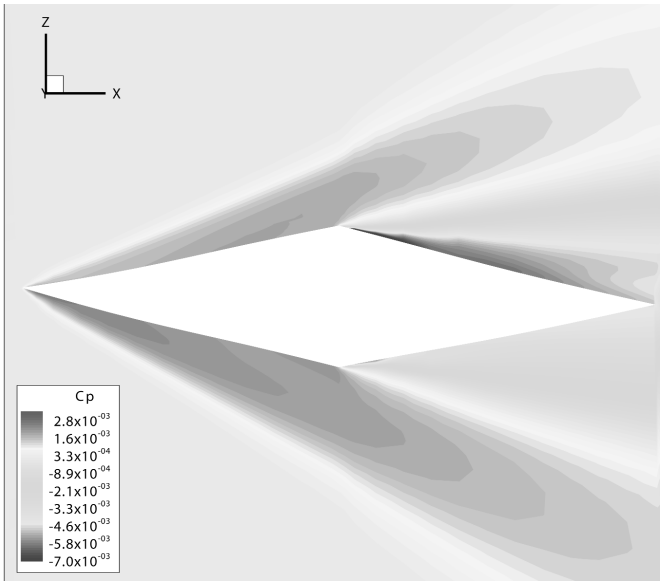


Figure 15. Pressure contours around the deformed typical section of the canted fin of the generic vehicle at M = 8·0, at 40,000ft, using Euler aerodynamics.

Table 2
Comparison of flutter boundaries for the generic vehicle at 40,000ft, obtained using different models for predicting aerodynamic loads

Aerodynamic model	7 modes M_f	7 modes k_ω	12 modes M_f	12 modes k_ω
Piston theory, linear	16·2	0·1215	13·2	0·1192
Piston theory, nonlinear	11·7	0·1344	7·1	0·3106
Euler, coarse mesh	11·6	0·1412	9·3	0·1714
Euler, refined mesh	11·2	0·1426	9·3	0·1626

The simulations in this study were carried out in parallel mode on nodes of a AMD cluster with Opteron processors. For the time-step size selected, the run time to obtain an aeroelastic transient response of the generic vehicle at 40,000ft using Euler aerodynamics was approximately 30 hours with five processors on the coarse mesh, and approximately 140 hours with nine processors on the refined mesh. The use of either seven or 12 structural modes did not significantly affect run time. A sample calculation carried out using Navier-Stokes aerodynamics required 36 days on nine processors when using the refined mesh.

5.0 CONCLUDING REMARKS

Based on the numerical results presented in this paper, the following conclusions can be gleaned.

1. For minimising run-time while retaining a sufficient level of accuracy, the mesh selected needs to have a careful placement of internal grid points depending on the flight condition. For hypersonic flow, the computational domain should not extend far beyond the body, with the majority of points placed close to the surface. Mesh convergence studies of both rigid and aeroelastic simulations might need to be carried out in order to select the optimal mesh.
2. For the generic vehicle, the aeroelastic model based on Euler solutions predicts a flutter boundary 31% higher than that predicted by third-order piston theory, due to the presence of significant three-dimensional flow effects captured by Euler aerodynamics. This leads to significant deformation of the canted fins, and different equilibrium configurations for the flexible vehicle are predicted by these two aerodynamic models. Hence, the surface pressure distributions are also found to be different. Since the aeroelastic transient solutions are calculated by considering small perturbations about these equilibrium positions, different aeroelastic behavior is predicted by these models.

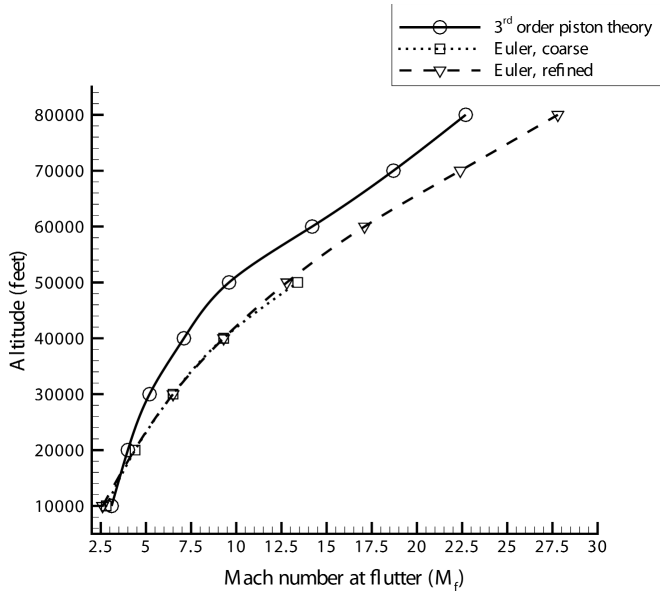


Figure 16. Flutter envelope of the generic hypersonic vehicle, calculated using piston theory and Euler aerodynamics.

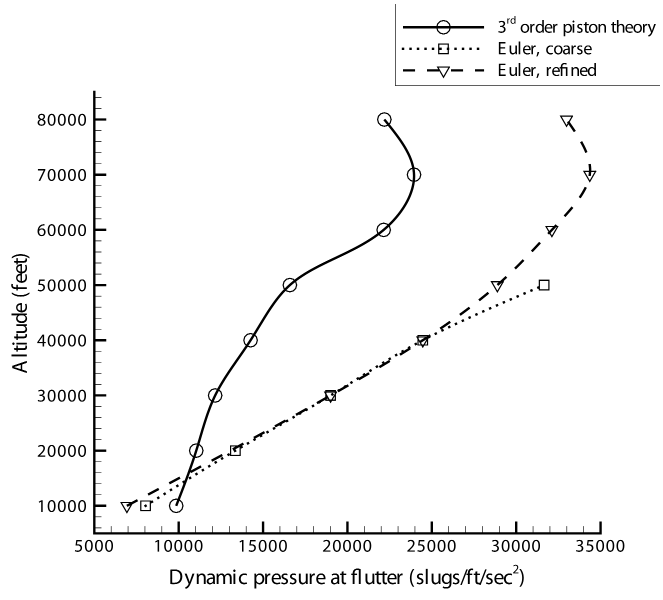


Figure 17. Dynamic pressure at flutter for the generic vehicle, calculated using piston theory and Euler aerodynamics.

https://doi.org/10.1017/S0001924000003420 Published online by Cambridge University Press

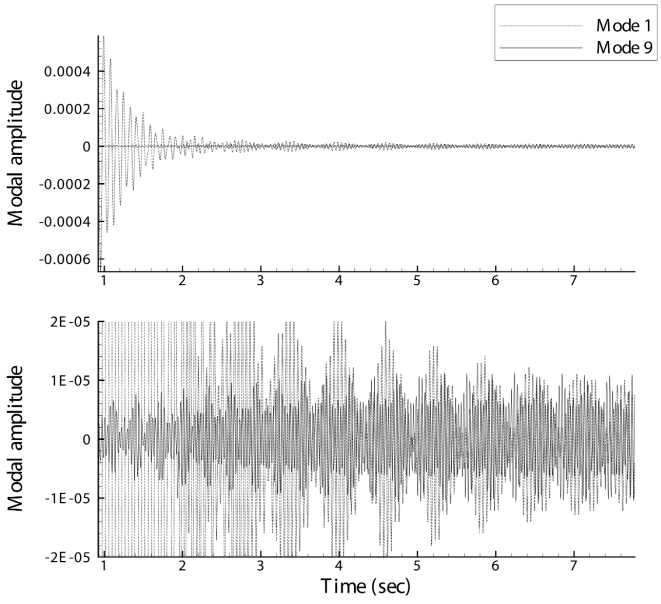


Figure 18. Aeroelastic transients for the generic vehicle at M = 28·0 and 80,000ft. Only modes one and nine are shown for clarity.

3. Based on the various aeroelastic simulations described in this study, it can be seen that the differences between approximate solutions based on third-order piston theory and more exact solutions based on Euler and Navier-Stokes aerodynamics can be small, or large, and these differences depend on the vehicle configuration and flight conditions.
4. The relatively low reduced frequencies observed for the generic hypersonic vehicle can be used to justify the quasisteady nature of piston theory loads. Also, such an approximation can also be used to increase computational efficiency when carrying out Euler or Navier-Stokes computations. This approach has been successfully explored in a recent paper.[48]

ACKNOWLEDGMENTS

The authors wish to express their gratitude to NASA Langley Research Center for the CFL3D code and thank Drs R. Bartels and R. Biedron for their help in using this code. This research has been supported both by AFOSR grant F49620-01-0158, with Dr. C. Allred as program manager, and NASA SVTI award NCC 3989, funded by NASA Marshall and Glenn Research Centers.

REFERENCES

1. BISPLINGHOFF, R.L. and DUGUNDJI, J. *Influence of Aerodynamic Heating on Aeroe-lastic Phenomena in High Temperature Effects in Aircraft Structures,* Pergamon Press, 1958, pp 288-312.
2. GARRICK, I.E. Aeroelasticity — frontiers and beyond, *J of Aircr*, 1976, **13**, pp 641-657.
3. HEDGEPETH, J.M. Flutter of rectangular simply supported panels at high supersonic speeds, *J of the Aero Sciences,* August 1957, **24,** (8), pp 563-573.
4. LAIDLAW, W.R. and WYKER, J.H. Potential aerothermoelastic problems associated with advanced vehicle design, *Aerospace Engineering,* January 1963, pp 154-164.
5. XUE, D.Y. and MEI, C. Finite element two-dimensional panel flutter at high supersonic speeds and elevated temperature, Proc. 31st AIAA/ASME/ASCE/AHS/ASC Structures, Structural Dynamics and Ma¬erials Conference, 1990, pp 1464-1475, AIAA Paper No. 90-0982.
6. GRAY, E.G. and MEI, C. Large-amplitude finite element flutter analysis of composite panels in hypersonic flow, Proc. 33rd AIAA/ASME/ASCE/AHS/ASC Structures, Structural Dynamics and Materials Conference, Dallas, TX, April 16-17 1992, pp 492-512, AIAA Paper No 92-2130.
7. ABBAS, J.F. and IBRAHIM, R.A. Nonlinear flutter of orthotropic composite panel under aerodynamic heating, *AIAA J*, 1993, **31,** (8), pp 1478-1488.
8. BEIN, T., FRIEDMANN, P., ZHONG, X. and NYDICK, I. Hypersonic flutter of a curved shallow panel with aerodynamic heating, Proc 34th AIAA/ASME/ASCE/AHS/ASC Structures, Structural Dynamics and Materials Conference, La Jolla, CA, April 19-22, 1993, AIAA Paper No. 93-1318.
9. NYDICK, I., FRIEDMANN, P.P. and ZHONG, X. Hypersonic panel flutter studies on curved panels, Proc 36th AIAA/ASME/ASCE/AHS/ASC Structures, Structural Dynamics and Materials Conference, New Orleans, LA, April 1995, pp 2995-3011, AIAA Paper no 95-1485.
10. MEI, C, ABDEL-MOTAGLY, K. and CHEN, R. Review of nonlinear panel flutter at supersonic and hypersonic speeds, *Applied Mechanics Reviews,* 1998.
11. RICKETTS, R., NOLL, T., WHITLOW, W. and HUTTSELL, L. An overview of aeroelasticity studies for the National Aerospace Plane, Proc. 34th AIAA/ASME/ASCE/AHS/ASC Structures, Structural Dynamics and Materials Conference, La Jolla, CA, April 19-22, 1993, , AIAA Paper No. 93-1313, pp 152 - 162.
12. SPAIN, C., ZEILER, T.A., BULLOCK, E. and HODGE, J.S. A flutter investigation of AU-moveable NASP-like wings at hypersonic speeds, Proc 34th AIAA/ASME/ASCE/AHS/ ASC Structures, Structural Dynamics and Materials Conference, La Jolla, CA, April 19-22, 1993, AIAA Paper No 93-1315.
13. SCOTT, R.C. and POTOTZKY, A.S. A method of predicting quasi-steady aerodynamics for flutter analysis of high speed vehicles using steady CFD calculations, Proc. 34th AIAA/ASME/ASCE/AHS/ASC Structures, Structural Dynamics and Materials Conference, La Jolla, CA, April 19-22, 1993, AIAA Paper No 93-1364, pp 595-603.
14. SPAIN, C., ZEILER, T.A., GIBBONS, M.D., SOISTMANN, D.L., POZEFSKY, P., DEJESUS, R.O. and BRANNON, C.R. Aeroelastic character of a National Aerospace Plane demonstrator concept, Proc 34th AIAA/ASME/ASCE/AHS/ ASC Structures, Structural Dynamics and Materials Conference, La Jolla, CA, April 19-22, 1993, pp 163-170.
15. RODGERS, J.P. Aerothermoelastic analysis of a NASP-like vertical fin, Proc 33rd AIAA/ASME/ASCE/AHS Structures, Structural Dynamics and Materials Conference, Dallas, TX, April 1992, AIAA-92-2400-CP.
16. HEEG, J., ZEILER, T., POTOTZKY, A., SPAIN, C. and ENGELUND, W. Aerothermoelastic analysis of a NASP demonstrator model, Proc 34th AIAA/ASME/ASCE/AHS/ ASC Structures, Structural Dynamics and Materials Conference, La Jolla, CA, April 19-22 1993, AIAA Paper No 93-1366, pp 617-627.
17. HEEG, J. and GILBERT, M.G. Active control of aerothermoelastic effects for a conceptual hypersonic aircraft, *J of Aircr*, 1993, **30,** pp 453-458.
18. BLADES, E., RUTH, M. and FUHRMAN, D. Aeroelastic analysis of the X-34 launch vehicle, Proc 40th AIAA/ASME/ASCE/AHS/ ASC Structures, Structural Dynamics and Materials Conference, St. Louis, MO, 1999, AIAA Paper No. 99-1352, pp 1321-1331.
19. FRIEDMANN, P.P., MCNAMARA, J.J., THURUTHIMATTAM, B.J. and NYDICK, I. Aeroelastic analysis of hypersonic vehicles, *J of Fluids and Structures*, 2004, **19,** pp 681-712.
20. GUPTA, K.K., VOELKER, L.S., BACH, C., DOYLE, T. and HAHN, E. CFD-based aeroelastic analysis of the X-43 hypersonic flight vehicle, 39th Aerospace Sciences Meeting & Exhibit, 2001, AIAA Paper No 2001-0712.
21. BERRY, S.A., HORVATH, T.J., HOLLIS, B.R., THOMPSON, R.A. and HAMILTON, H.H. X-33 hypersonic boundary layer transition, 33rd AIAA Thermophysics Conference, Norfolk, VA, 28 June - 1 July 1999, AIAA Paper No. 99-3560.
22. RILEY, C.J., KLEB, W.L.,and ALTER, S.J. Aeroheating predictions for X-34 using an inviscid-boundary layer method, 36th Aerospace Sciences Meeting & Exhibit, Reno, NV, January 1998, AIAA Paper No. 98-0880.
23. MCNAMARA, J.J. and FRIEDMANN, P.P. Aeroelastic and aerothermoelastic analysis of hypersonic vehicles: current status and future trends, Proceedings of the 48th AIAA/ASME/ASCE/AHS/ASC Structures Structural Dynamics and Materials Conference, Honolulu, Hawaii, April 23-26, 2007, AIAA Paper No. 2007-2013.
24. MCNAMARA, J.J., FRIEDMANN, P.P., POWELL, K.G, THURUTHIMATTAM, B. and BARTELS, R.E. Aeroelastic and aerothermoelastic behavior in hypersonic flow, *AIAA J,* October 2008, **46,** (10), pp 2591- 2610.

https://doi.org/10.1017/S0001924000003420 Published online by Cambridge University Press

25. KRIST, S.L., BIEDRON, R.T. and RUMSEY, C.L. CFL3D User's Manual (Version 5.0), NASA, TM 1998-208444, 1997.
26. BARTELS, R.E. Mesh strategies for accurate computation of unsteady spoiler and aeroelastic problems, *J of Aircr*, May 2000, **37,** (3), pp 521-525.
27. ROBINSON, B.A., BATINA, J.T. and YANG, H.T. Aeroelastic analysis of wings using the Euler equations with a deforming mesh, *J of Aircr,* November 1991, **28,** pp 778-788.
28. CUNNINGHAM, H.J., BATINA, J.T. and BENNETT, R.M. Modern wing flutter analysis by computational fluid dynamic methods, *J of Aircr,* 1989, **25,** (10), pp 962-968.
29. BATINA, J.T. Unsteady Euler airfoil solutions using unstructured dynamic meshes, *AIAA J*, 1990, **28,** pp 1381-1388.
30. TEZDUYAR, T.E., BEHR, M. and LIOU, J. A new strategy for finite element computations involving moving boundaries and interfaces — The deforming-spatial-domain/space-time procedure: I. the concept and the preliminary numerical tests, *Computer Methods in Applied Mech and Eng,* 1992, **94,** pp 339-351.
31. HUGHES, T.J.R. and HULBERT, G.M. Space-time finite element methods for elastodynamics: formulations and error estimates, *Computer Methods in Applied Mech and Eng,* 1988, **66,** pp 339-363.
32. PATIL, M.J., HODGES, D.H. and CESNIK, C.E.S. Nonlinear aeroelastic analysis of complete aircraft in subsonic flow, *J of Aircr*, September 2000, **37,** (5), pp 753-760.
33. DONEA, J., GUILIANI, S. and HALLEUX, J.P. An arbitrary Lagrangian-Eulerian finite element method for transient dynamic fluid-structure interactions, *Computer Methods in Applied Mech and Eng,* 1982, **33,** pp. 689-723.
34. BENDIKSEN, O.O. A new approach to computational aeroelasticity, Proc. AIAA/ASME/ASCE/AHS/ASC 32nd Structure, Structural Dynamics and Materials Conf, Baltimore, MD, 8-9 April, 1991, AIAA Paper 91-0939, pp 1712-1727.
35. FARHAT, C, LESOINNE, M. and MAMAN, N. Mixed explicit/implicit time integration of coupled aeroelastic problems: three-field formulation, geometric conservation and distributed solution, *Int J for Numerical Methods in Fluids,* 1995, **21,** pp 807-835.
36. IRAN H. and FARHAT, C. An integrated platform for the simulation of fluid-structure-thermal interaction problems, Proc. 43rd AIAA/ASME/ASCE/AHS Structures, Structural Dynamics and Materials Conference, Denver, CO, April 2002, AIAA Paper No 2002-1307.
37. STEPHENS, C.H., ARENA, A.S. and GUPTA, K.K. Application of the transpiration method for aeroservoelastic prediction using CFD, Proc. of the 39th AIAA/ASME/ASCE/AHS/ASC Structures, Structural Dynamics, and Materials Conference and Exhibit, Long Beach, CA, April 20-23, 1998, AIAA Paper 98-2071.
38. HARTWICH, P. and AGRAWAL, S. Perturbing multiblock patched grids in aeroelastic design optimization applications, June 1997, AIAA Paper 97-2038.
39. BARTELS, R.E., RUMSEY, C.L. and BIEDRON, R.T. CFL3D Ver. 6.4–General Usage and Aeroelastic Analysis, 2006, NASA TM-2006-214301.
40. BARTELS, R.E. Finite macro-element mesh deformation in a structured multi-block Navier–Stokes code, 2005, NASA TM -2005-213789.
41. THOMPSON, J., BHARAT, S. and WEATHERRILL, N. *Handbook of Grid Generation*, CRC Press, Boca Raton, FL, 1998.
42. *MSC/NASTRAN Basic Dynamic Analysis User's Guide*, Los Angeles, The MacNeal-Schwendler Corporation, 1998.
43. BOUSMAN, W.G. and WINKLER, D.J. Application of the moving-block analysis, Proceedings of the AIAA Dynamics Specialist Conference, Atlanta, GA, April 1981, pp 755-763, AIAA Paper No 81-0653.
44. NYDICK, I. Studies in Hypersonic Aeroelasticity, PhD Dissertation, University of California, Los Angeles, 2000.
45. THURUTHIMATTAM, B.J. Fundamental Studies in Hypersonic Aeroelasticity Using Computational Methods, PhD Dissertation, The University of Michigan, 2005.
46. LIGHTHILL, M.J. Oscillating airfoils at high Mach numbers, *J of the Aero Sciences,* June 1953, **20,** (6).
47. ASHLEY, H. and ZARTARIAN, G. Piston theory — a new aerodynamic tool for the aeroelastician, *J of the Aero Sciences,* 1956, **23,** (12), pp 1109-1118.
48. MCNAMARA, J.J., FRIEDMANN, P.P., CROWELL, A.R. and GOGULAPATI, A. Reduced order modeling of unsteady hypersonic aerodynamics, International Forum on Aeroelasticity and Structural Dynamics, Seattle, WA, June 21-25, 2009, IFASD Paper 2009-031.

https://doi.org/10.1017/S0001924000003420 Published online by Cambridge University Press